AIAA JOURNAL
Vol. 47, No. 11, November 2009

Proper Orthogonal Decomposition Analysis of Separated and Reattached Pressure Gradient Turbulent Flows

Mohammad K. Shah* and Mark F. Tachie†
University of Manitoba, Winnipeg, Manitoba R3T 5V6, Canada

DOI: 10.2514/1.40095

In this paper, the proper orthogonal decomposition was used to analyze velocity data obtained in turbulent flow downstream of a transverse square rib attached to the lower walls of parallel-walled asymmetric diverging and converging channels. The velocity measurements were obtained using a particle image velocimetry. The proper orthogonal decomposition results demonstrate that the energetic structures in the flow contribute most to Reynolds shear stress and least to transverse normal stress. The implications of these observations to the large-scale anisotropy are discussed. Significant differences are observed in the reconstructed Reynolds stress profiles at the center of the separated shear layer and those close to the reattachment point. The results also indicate that contribution of the energetic structures to the Reynolds stresses is higher at the upstream section of the ribs than in the separated layer. This was attributed to a more uniform energy distribution among the proper orthogonal decomposition modes in the separated shear layer than in the upstream section. The distributions of the mean velocity, mixing length, and eddy viscosity at selected locations were also analyzed. The mixing-length profiles in the inner region of the separated shear layer do not follow the well-documented linear profile reported for simple near-wall turbulent flows.

I. Introduction

SEPARATED and reattached flows have been the subject of intense research due to their practical importance in diverse fluid engineering applications. For example, flows over and around wall-mounted obstacles or through orifices are frequently encountered in practice, examples being heat exchangers and combustors. Separated and reattached flows are also used as a prototypical shear flow to conduct fundamental near-wall turbulence research. A wide range of simple laboratory geometries such as the backward-facing step (Bradshaw and Wong [1]), forward-facing step (Abu-Mulaweh [2]), transverse square rib (Abdalla et al. [3]), splitter plate (Ruderich and Fernholz [4]), and blunt plate (Kiya and Sasaki [5]) have been used to study separated and reattached flows. These studies have shed light on the different regimes of the flow according to Reynolds number and boundary conditions (aspect ratio, blockage, freestream turbulence intensity, etc.). The investigations have been conducted using various pointwise techniques such as hot wire and laser Doppler anemometry and whole-field techniques such as particle image velocimetry (PIV). In most of these studies, the mean velocities and one-point turbulent statistics were obtained to study the salient features of the velocity field. A summary of previous studies on separated reattached flows, their Reynolds number, experimental technique, and relevant quantities are summarized by Shah [6] and Shah and Tachie [7].

The existence of coherent structures is one of the most important features of the turbulent flows (Kline et al. [8]). The essential flow physics are believed to be buried within coherent structures or eddies that are characterized by organized motions. It is generally believed that a better understanding of coherent structures is the key to understanding turbulence and its control (Kostas et al. [9]). An in-depth knowledge of coherent structures would also offer the possibility of clarifying the physical mechanism through which turbulent energy is dissipated into heat. The implications for turbulence control include the reduction of the skin friction in wall-bounded flows, the delay of separation in wake flows, and the enhancement of mixing in free shear. In spite of concerted research on coherent structures over the past decades, they are relatively less understood compared with one-point turbulent statistics. As rightly noted by Moin and Moser [10], the present knowledge of organized motions has seldom been used in turbulence theories or quantitative models of turbulence. This was attributed to lack of quantitative definition of organized structures and an objective means for assessing their contribution to turbulence stresses and their importance in the production of turbulence.

The process of identifying and describing coherent structures has been a very challenging undertaking because they are, more often than not, hidden among the incoherent turbulent motions (Kostas et al. [9]). With the advent of increasing computing power, a large volume of flow data can now be collected to study turbulence in its full complexity. Hence, to extract the most useful structural information about the physical processes, this large volume of data must be summarized in a concise manner. A variety of statistical techniques such as two-point correlation and conditional or phase-averaging techniques have been used to study coherent structures (Moin and Moser [10]). The proper orthogonal decomposition (POD) has emerged as a powerful statistical technique for extracting dominant features and identifying coherent structures. The POD technique is first introduced in turbulence research by Lumley [11], in an attempt to systematically identify coherent structures in the turbulent flows, and subsequently by Sirovich [12] and Berkooz et al. [13]. The POD can effectively compress and summarize large quantities of data so that the most useful information about the physical processes occurring may be extracted (Kostas [14]). More important, the contribution of the extracted eddies to turbulence stresses and turbulence production can be determined.

In principle, the POD decomposes a series of experimental or numerical measurements into a number of modes that make up an orthonormal basis spanning the entire data set. The POD captures the most energetic and hence largest structures of the flow in the first modes. In other words, if the dynamics of the flow is dominated by a few large flow structures, the data can be represented satisfactorily using only a few of the first modes. The POD analysis requires the knowledge of two-point spatial correlation function. This would require the use of multipoint measurement techniques such as rakes

Presented as Paper 4347 at the 5th AIAA Theoretical Fluid Mechanics Conference, Seattle, WA, 8 June 2023–8 June 2026; received 28 July 2008; revision received 10 February 2009; accepted for publication 18 February 2009.

*Mechanical Engineer, DBR Technology Centre, Schlumberger, 9450 17th Avenue, Edmonton, Alberta T6N 1M9, Canada. Student Member AIAA.

†Professor, Mechanical and Manufacturing Engineering Department, 75A Chancellors Circle. Member AIAA.

of hot wires and PIV. Because the PIV is a nonintrusive whole-field measurement technique, it is well suited for POD analysis.

The POD has been implemented in many types of flows, such as jets, boundary layers, and backward-facing step flows. In most of the studies, the fluctuating velocity fields were analyzed, assuming that the large-scale coherent structures contain the main fraction of the turbulent kinetic energy. For example, Reichert et al. [15] observed that for turbulent flow in a square channel, the first 100 POD modes contain over 95% of the turbulent kinetic energy and the first 10 modes captured over 50% of the total energy. Subdomain modes were able to capture more of their domain's total energy. In other words, the subdomain decomposition was found to be more effective than full domain decomposition. The relatively small-scale structures were only captured when the number of modes was increased to about 100. It was found that the first mode contributed more to $\langle -uv \rangle$ than to kinetic energy. The more recent direct numerical simulation (DNS) study reported by Alfonsi and Primavera [16] showed that the first 16 modes contribute about 20% of the total energy, and 6.9% of the energy resides in the first three modes.

Moin and Moser [10] applied DNS and POD to study fully developed channel flow. It was found that the contribution of the dominant modes to Reynolds shear stress is significantly higher than to turbulent kinetic energy. They reported that the convergence to the energy and the turbulent intensities is monotonic, however; there is no such guarantee for the Reynolds shear stress. This is because POD is optimum for the convergence of turbulent kinetic energy. It was expected that the convergence of the POD expansion in subdomain is better than the whole domain. Sen et al. [17] carried out POD analysis of DNS data obtained over a smooth surface and for flow over egg-carton roughness using 6000 realizations. Contribution of the first few modes to total energy is higher for smooth-wall than for rough-wall flow. They suggested that the slow convergence of POD modes obtained for a rough wall indicated an increase in the range of length scales. Profiles of turbulent intensities and Reynolds shear stress converge toward the time-averaged statistics faster in the inner region than in the outer region.

Kostas et al. [9,18] performed POD analysis on both the fluctuating velocity and vorticity fields of a backward-facing step at two Reynolds numbers ($Re_k = 580$ and 4660). They used 1024 PIV realizations in the x–y plane to perform the POD analysis. Large-scale structures seem to be largely responsible for the persistence of $\langle u^2 \rangle$ and $\langle -uv \rangle$ in the flow downstream of the reattachment, whereas $\langle v^2 \rangle$ is governed predominantly by the fine-scale structures. For this reason, both the spatial distribution and the peak value of $\langle -uv \rangle$ were recovered by using approximately 50 modes, but $\langle v^2 \rangle$ requires modes in excess of 50 to recover the peak value.

Orellano and Wengle [19] reported POD analysis of the large eddy simulation data at $Re_k = 3000$ over a fence in forced and unforced flow using 6000 realizations. They reported that 2000 POD modes represented 99% of turbulent kinetic energy, and 20 modes represent about 25% of the turbulent kinetic energy for the unforced flow. The POD analysis of the transverse velocity component indicated the formation of a mainly 2-D vortex shedding from recirculation zone. The results reveal that the shedding of large-scale structures from the recirculation bubble behind the obstacle is the dominant process downstream of the fence in the unforced flow.

This paper is part of experimental research program to study the salient features of separated and reattached flows in nearly zero pressure gradient, adverse pressure gradient (APG), and favorable pressure gradient (FPG). The experiments were performed in a parallel-walled channel (CC), asymmetric diverging channel (APG), and asymmetric converging channel (FPG). The velocity measurements were conducted using a high-resolution planar PIV. From the PIV data, the boundary-layer parameters, mean velocities, turbulent intensities, Reynolds stresses, triple-velocity correlations, and terms in the transport equations for turbulent kinetic energy and Reynolds shear stress were obtained. These results were reported and discussed by Shah [6] and Shah and Tachie [20]. In the first part of the present paper, the mean velocity, Reynolds shear stress, and transport and mixing properties of the separated and reattached flows in various pressure gradients are reported. This is then followed by application of the POD technique to document the salient features of the large-scale or dominant structures and to study their contribution to the turbulent kinetic energy and Reynolds shear stress. Further insight into the flow structures is gained by reconstructing the flow with increasing number of POD modes.

II. Experimental Setup and Measurement Procedure

A. Test Sections and Measurement Procedure

The experiments were performed in a parallel-walled channel, an asymmetric diverging channel, and an asymmetric converging channel, hereafter referred to as tests CC, APG, and FPG, respectively. These channels as well as the PIV system employed in the present study and the measurement procedure are described extensively by Shah [6] and Shah and Tachie [20]. Therefore, only the salient features of the test facility and measurement procedure are presented in this paper. The channels were inserted into an existing water channel with test section that is 2500 mm long, 200 mm wide, and 200 mm deep. As shown in Fig. 1a, the CC channel is 2500 mm long and has a half-channel height $h = 34.5$ mm. For the APG and FPG channels (Figs. 1b and 1c), the first 1000 mm (OA) and the last 500 mm (BC) sections have straight parallel walls, whereas the 1000 mm section (AB) located between these parallel sections diverges nonlinearly from a height of 54 to 84 mm for the APG case and converges from 84 to 54 mm for the FPG case. The zero location for the x coordinate ($x = 0$) is taken at 1000 mm from the inlet of the test section, which also marks the start of convergence/divergence (A), $y = 0$ on the lower wall, and $z = 0$ at the midplane of the channel. The heights of the variable channel for APG and FPG are, respectively, given by

$$2h(x) = 54 - 7.39 \times 10^{-4}x + 5.73 \times 10^{-5}x^2 - 3.12 \times 10^{-9}x^3 - 5.09 \times 10^{-11}x^4 + 2.78 \times 10^{-14}x^5 \quad (1a)$$

$$2h(x) = 84 - 4.01 \times 10^{-2}x + 2.09 \times 10^{-5}x^2 - 7.17 \times 10^{-8}x^3 + 8.83 \times 10^{-11}x^4 - 2.78 \times 10^{-14}x^5 \quad (1b)$$

where x is measured in millimeters and the relationship is valid in the range of $0 \leq x \leq 1000$.

The flow was seeded with 5 μm polyamide seeding particles having a specific gravity of approximately 1.03. An Nd-YAG laser (120 mJ/pulse) of 532 nm wavelength was employed to illuminate the flowfield. The laser sheet was located at the midplane of the channel. A 12-bit HiSense 4M camera was coupled to a 60 mm AF Micro Nikkor lens. The sampling rate of the image pairs was 5.8 Hz. The instantaneous digital images were postprocessed by the adaptive-correlation option of the commercial software developed by Dantec Dynamics (FlowManager 4.50.17). A detailed convergence test and the effects of spatial resolution on the mean velocities and turbulent statistics were conducted and reported by Shah and Tachie [7]. Based on those results, a sample size of 2040 images and an interrogation area of 32×16 pixels with 50% overlap were used to compute the mean velocity and turbulent statistics reported subsequently. There are many sources of measurement uncertainty in PIV measurements. The guidelines and steps necessary to minimize these errors are discussed by Prasad et al. [21] and Forliti et al. [22]. Typical measurement uncertainty in the instantaneous velocity field is of the order 0.05 to 0.1 pixels. Following the methodologies proposed and explained by Coleman and Steele [23], the uncertainty in the mean velocities at 95% confidence level was determined to be $\pm 2\%$. The uncertainties in Reynolds shear stress, mixing length, and eddy viscosity were estimated to be ± 10, ± 15, and $\pm 15\%$, respectively. In the graphs shown subsequently, error bars are used to indicate the measurement uncertainties at 95% confidence level.

B. Test Conditions

A 75-mm-wide trip made of four 3-mm-wide rectangular bars, 21 mm apart, was used on the upper and lower walls of the channel

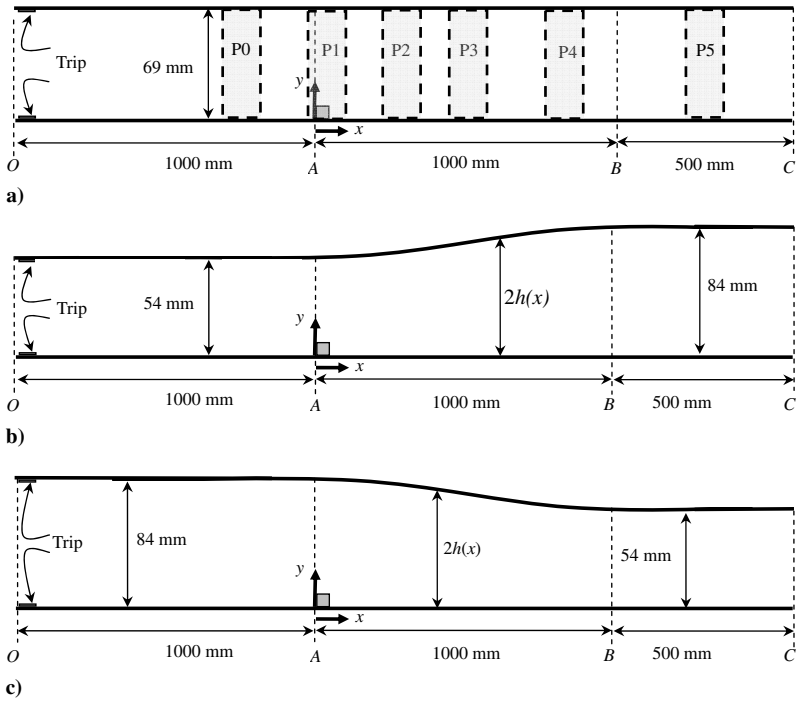

Fig. 1 Experimental setup: a) parallel-walled channel, b) diverging channel, and c) converging channel. Note that dashed regions, P0 to P5, denote *x*–*y* planes in which PIV measurements were made for a channel (not to scale).

entrance to ensure a rapid development of the turbulent boundary layer. The two-dimensional square rib of height $k = 6$ mm was glued to the bottom of the channel at $x = 0$ (1000 mm from the inlet of a given channel) to cause flow separation for the three cases. For each test condition (i.e., tests CC, APG, and FPG), reference measurements were made in an x–y plane upstream of the rib (denoted as P0 in Fig. 1a) to characterize the approach flow and then in five planes (P1–P5) located around and downstream of the rib. For a given test case, the plane of measurement is indicated with a hyphen. For example, test APG-P1 refers to the flow downstream of a rib in the diverging channel and P1 indicates the plane containing the rib. A summary of some of the upstream parameters is presented in Table 1. For a given test condition, U_{eo} is the maximum streamwise velocity, δ_o is the boundary-layer thickness defined as the y location at which the local velocity is 99% of U_{eo}, δ_o^* is the displacement thickness, θ_o is the momentum thickness, H_o is the shape factor, Re_k is the Reynolds number based on U_{eo} and k, Re_θ is Reynolds number based on U_{eo} and θ_o, and k/δ_o is the perturbation strength. Note that a subscript o is used to describe upstream parameters. The boundary-layer thickness as well as the displacement and momentum thicknesses of the approach flow are nearly the same in test CC and test APG. The shape parameters obtained for the three test cases are similar and compare reasonably well with prior data at similar Re_θ (Purtell et al. [24]). The perturbation strength k/δ_o of 0.31, 0.29, and 0.15, respectively, in tests CC, APG, and FPG implies a strong perturbation according to the classification proposed by Bradshaw and Wong [1]. The blockage ratio $k/(2h)$, where $2h$ is the channel height at $x = 0$ and the ratio of the rib height to the viscous length scale of the approach flow ($k^+ = kU_{\tau o}/\nu$, where $U_{\tau o}$ is the friction velocity evaluated at the upstream section, P0) are also summarized in Table 1. Note that the crest of the rib is well within the logarithmic layer in all of the tests. Because $k^+ = 140$ in tests CC, APG, and FPG, it implies that the distortion of the inner layer of the approach boundary layer by the rib is identical in all of the tests. The variation of the boundary-layer parameters as well as acceleration and deceleration parameters downstream of the rib is reported by Shah [6] and Shah and Tachie [20]. Furthermore, the values and accuracy of skin-friction coefficient in the redevelopment region are discussed in those studies as well. Therefore, those results are not repeated here.

III. Mean and Turbulent Quantities

A. Mean Streamwise Velocity Profiles

Profiles of mean velocity, turbulent intensities, Reynolds shear stress, third-order moments, and budget terms in the separated and redevelopment region have been discussed in detail by Shah [6] and Shah and Tachie [7,20]. The two-dimensionality of the mean flow within the separated and reattached region was also verified by Shah [6]. As reported in those studies, the flow dynamics in the upper boundary layer of the separated region and early stage of flow redevelopment were insensitive to pressure gradient. Note that the term *lower boundary layer* is used to describe the profile formed on the lower wall up to the location of local maximum mean velocity U_e, and *upper boundary layer* is from the upper wall to the location of U_e. On the other hand, significant differences were observed in the lower boundary layer among the three test cases. Hence, only profiles in the lower boundary layer are reported in this study. Typical profiles obtained in the variable sections of the FPG channel (at $x/k = 224$) and APG channel (at $x/k = 205$) without the rib on the lower wall from Shah and Tachie [25] are compared with those obtained at $x/k = 200$ in the present study. Although the x/k locations are not identical in the previous and present studies, the comparison is still invaluable.

The mean streamwise velocity profiles at selected x/k locations are shown in Fig. 2a. In this and subsequent plots, y is normalized by the local boundary-layer thickness δ, and the mean velocity or

Table 1 Summary of upstream flow parameters

Test	U_{eo}, m/s	δ_o, mm	δ_o^*, mm	$\theta_o$mm	H_o	Re_k	Re_θ	k/δ_o	$k/2h$	$k^+ = kU_{\tau o}/\nu$
CC	0.445	19	2.2	1.4	1.57	2640	620	0.31	0.09	140
APG	0.460	21	2.8	1.8	1.55	2760	830	0.29	0.11	140
FPG	0.464	39	3.6	2.5	1.44	2760	1150	0.15	0.07	140

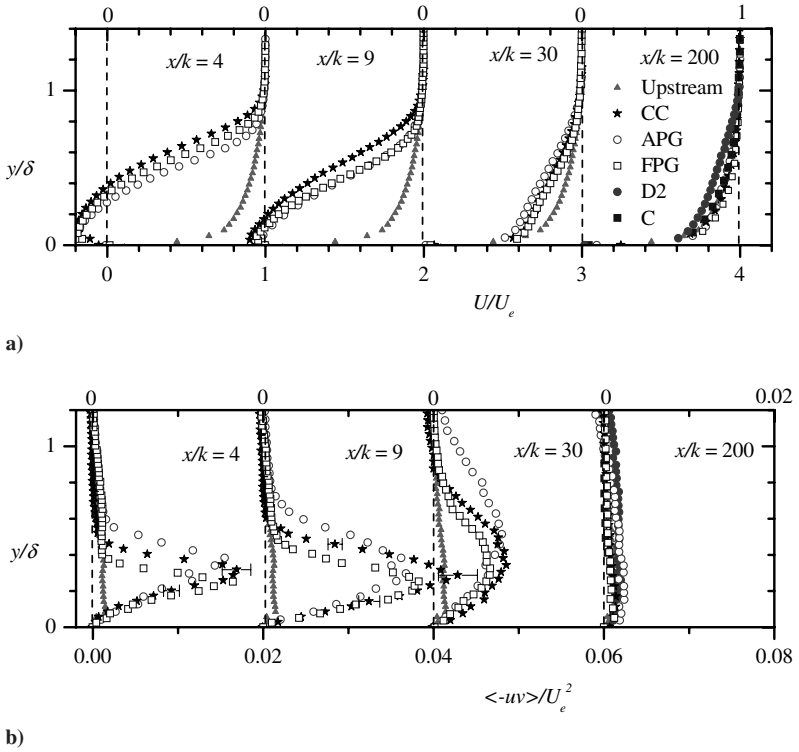

Fig. 2 Streamwise mean velocity and Reynolds shear stress profiles at various streamwise locations: a) U/U_e and b) $\langle -uv \rangle / U_e^2$. Test *D2* is at $x/k = 205$ (*L5*), and test *C* is at $x/k = 224$ (*L5*). Note that local boundary-layer thickness and local maximum streamwise velocity are used as length and velocity scales, respectively.

turbulent quantities are normalized by the local maximum value of U (i.e., U_e). As expected, the presence of the rib reduced the values of U close to the lower wall considerably. Consequently, the lower boundary-layer profiles downstream of the rib become less uniform compared with the reference upstream profile (APG-P0). The maximum backflow is approximately $0.2U_e$ for all of the test cases. This value is similar to those reported in previous separated and reattached flows downstream of a forward-facing step (Tachie et al. [26]) and backward-facing step (Eaton and Johnston [27]). The mean velocity recovered back toward the upstream profile at $x/k = 200$. As expected, the recovery process is slowest in test APG. The profiles obtained at $x/k = 200$ in the FPG (with or without ribs) are nearly indistinguishable. In APG, on the other hand, the present profiles are in better agreement with the reference upstream profile than if no rib was attached to the floor.

The Reynolds shear stress profiles are plotted in Fig. 2b. It was observed that, irrespective of the pressure gradient, the turbulence level rises consistently until $x/k = 9$ (which is approximately one step height upstream of the reattachment point). The peak values of $(\langle -uv \rangle / U_e^2)_{\max}$ at $x/k = 9$ of test APG, test FPG, and test CC are about 10 times as high as the upstream value. The region of enhanced turbulence levels coincides with the flow region of strong shear layer in Fig. 2a. As the flow evolves downstream of the rib and the shear layer propagates outward from the lower wall, so does the region of high turbulence levels. At $x/k = 200$, the profiles in test CC collapsed reasonably well on to the corresponding upstream profile. On the other hand, profiles obtained in the FPG are lower than the upstream profiles, whereas those obtained in APG are still higher than the upstream profiles. These observations are valid for the profiles for pressure gradient flows with and without the rib.

B. Profiles of Mixing Length and Eddy Viscosity

The methodology of modeling turbulent flows via mixing length $l_m = (\langle -uv \rangle)^{0.5} / (\partial U / \partial y)$ and eddy viscosity $\nu_t = \langle -uv \rangle / (\partial U / \partial y)$ is one of the simplest and easiest to implement in all turbulence models (Wilcox [28]). Even though they fail to incorporate the exact physical processes, they have been successful in predicting some of the flow characteristics in simple shear flows. In the inner region ($y/\delta < 0.2$) of canonical boundary layer and channel flows, the mixing length follows the universal relation $l_m = \kappa y$ (where $\kappa = 0.41$ is the von Kármán constant). In turbulence models, a constant value of 0.09δ (where δ is the local boundary layer) is normally used for canonical boundary layers in the outer region. This is also the value recommended, for example, in the turbulence model proposed by Johnson and King [29].

The distributions of mixing length at selected x/k locations in the separated and redevelopment regions are shown in Figs. 3a–3d. The upstream profile follows the universal relation in the inner region. In the outer region, the upstream profile increases continuously, likely because of the low Reynolds number effects as well as the depressed wake observed in the log-law plots (Shah and Tachie [20]). In such a case, $\partial U / \partial y$ tends to zero more rapidly than $\langle -uv \rangle$ does, producing relatively higher l_m values than in canonical boundary layers at moderate and high Reynolds numbers.

Figure 3a shows that in the separated region ($x/k = 4$), the linear region observed in canonical near-wall turbulent flows does not exist. Furthermore, the profiles attain a near-constant value in the outer region, but this value is lower than $l_m = 0.09\delta$ for canonical near-wall turbulent flows. These results imply that turbulence models based on the mixing-length approach would fail to accurately predict the flow characteristics in the separated region. In the early stages of flow redevelopment ($x/k = 30$), a linear region is established in the inner region, but the slope is about twice the value of $\kappa = 0.41$ observed in the upstream profile. In the outer region, the profiles begin to increase above the value of 0.09δ. The results also imply that the Reynolds shear stress is decaying more slowly than the mean shear ($\partial U / \partial y$). Further downstream, the slope in the inner region has reduced to 0.41, suggesting complete recovery in the inner region. Similar to the results obtained in the APG without a rib, the mixing length decays in the outer region compared with the upstream profile due to higher characteristic values of $\partial U / \partial y$.

The distributions of the eddy viscosity are shown in Figs. 3e–3h. The profiles obtained downstream of the rib are higher than the upstream profile. It appears that the slope in the near-wall region gradually increases downstream of the rib ($x/k = 30$). It is observed that the eddy viscosity in the outer part of the flow also rises initially

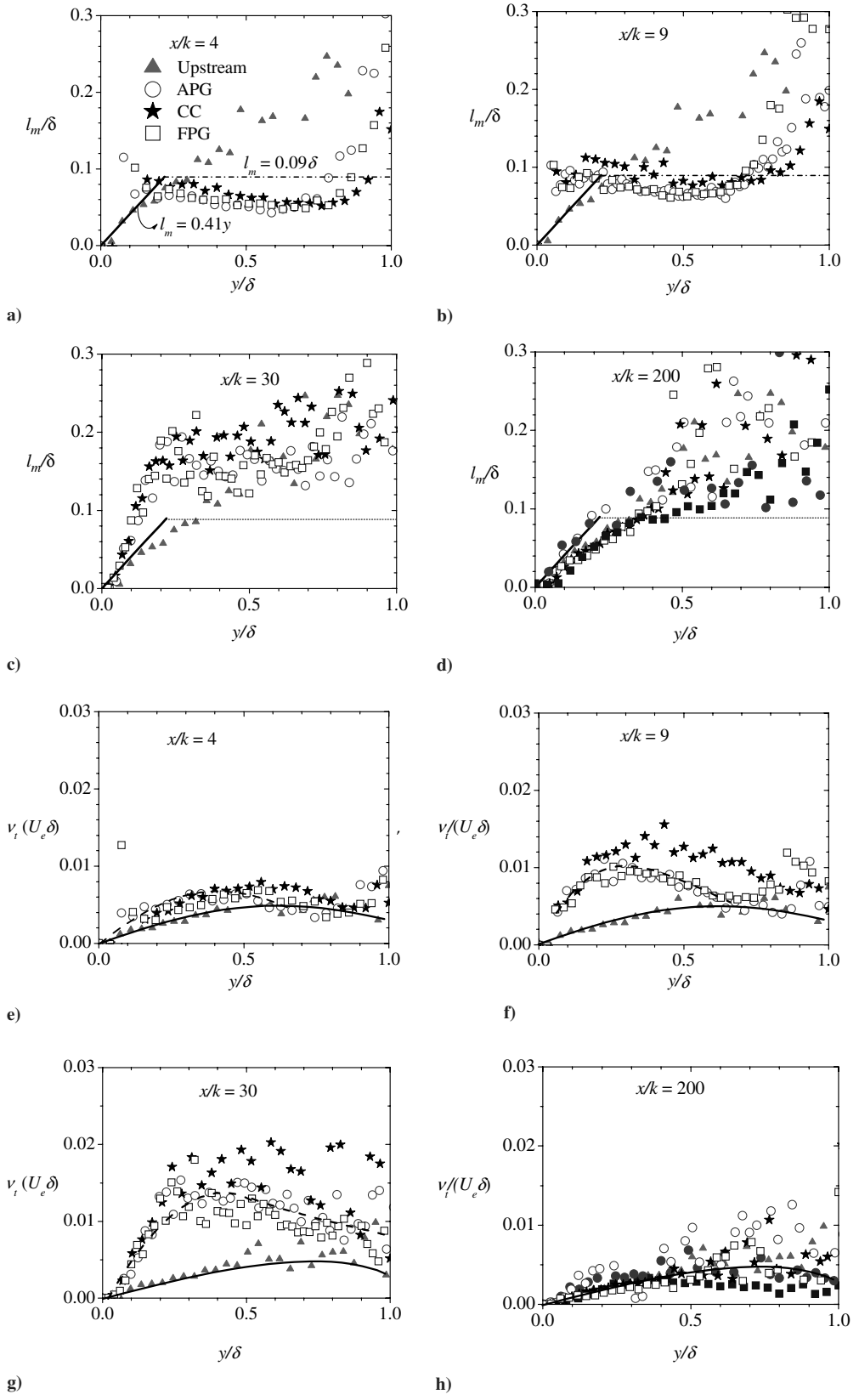

Fig. 3 Profiles of mixing length and eddy viscosity at selected locations. At location $x/k = 200$, reference test $D2$ (●) is at $x/k = 205$ ($L5$), and test C (■) is at $x/k = 224$ ($L5$). Solid lines denote $l_m = \kappa y$ and dash-dot lines denote $l_m/\delta = 0.09$. Note that local boundary-layer thickness and local maximum streamwise velocity are used as length and velocity scales, respectively.

in the region $x/k < 30$ and subsequently begins to decay farther downstream. These high values of the eddy viscosity in the outer parts of the flow far downstream indicate that $\partial U/\partial y$ is decaying more rapidly than the shear stress.

IV. Application of POD to the Experimental Data

A detailed discussion and implementation of the snapshot POD technique is provided by Shah [6] and references provided therein. In this section, an overview of the snapshot POD technique is described.

Subsequently, the POD is applied to the experimental data to analyze and interpret the dominant structures in the separated and reattached turbulent flows. As shown in Sec. III, the effects on the mean and turbulent quantities in the separated as well as the early reattachment region were most significant in the lower half of the channel. For all test cases considered in this section, the POD analysis was applied to the flow regions $y/k \leq 6$, which encompass the lower boundary layer. The confinement of the analysis to the lower boundary layer also reduced the computational effort considerably.

A. Implementation of POD

The snapshot POD method proposed by Sirovich [12] is employed in the present study. In this case, each instantaneous PIV data is considered to be a snapshot of the flow, and the total number of snapshots is denoted by N. The total number of vectors in each velocity field (snapshot) is M. The snapshot method is computationally efficient in the case of PIV measurements in which $M \gg N$. For the two-dimensional flow domain considered in this study, the snapshot POD analysis concerns the fluctuating parts of the velocity components (u_j^n, v_j^n), where u and v denote the fluctuating part of the velocity components in the streamwise and transverse directions, respectively. The index n runs through the N snapshots and j runs through the M positions of velocity vectors in a given snapshot [i.e., $u_j = u(x_j, y_j)$]. Note that the fluctuating velocity components were obtained by subtracting the ensemble-averaged snapshot from each member of the instantaneous velocity field. The ensemble-averaged snapshot is often considered to be the zeroth mode of the POD.

The present snapshot analysis follows the procedure outlined by (Meyer et al. [30]). As described by Shah [6], all of the fluctuating velocity components from the N snapshots are arranged in a matrix $\boldsymbol{U}$. The $N \times N$ autocovariance matrix is obtained from $\boldsymbol{C} = \boldsymbol{U}^T\boldsymbol{U}$. A set of N eigenvalues $\boldsymbol{\lambda}^i$ and a corresponding set of orthonormal eigenvectors $\boldsymbol{A}^i$ that satisfy $\boldsymbol{C}\boldsymbol{A}^i = \boldsymbol{\lambda}^i\boldsymbol{A}^i$ can be evaluated from the autocovariance matrix, where i spans from 1 to N. Here, the eigenvalues are ordered by decreasing value as follows: $\boldsymbol{\lambda^1} > \boldsymbol{\lambda^2} > \cdots > \boldsymbol{\lambda}^N > 0$. The normalized POD modes ϕ^i are constructed from the projection of the eigenvectors $\boldsymbol{A}^i$ on the original fields as follows:

$$\boldsymbol{\phi}^i = \frac{\sum_{n=1}^{N} A_n^i \boldsymbol{u^n}}{\left\| \sum_{n=1}^{N} A_n^i \boldsymbol{u^n} \right\|}, \qquad \boldsymbol{i} = 1, \ldots, N \tag{2}$$

where A_n^i is the nth component of the eigenvector corresponding to λ^i and $\| \cdot \|$ is the L_2-norm. The expansion or POD coefficients a_i of each mode were calculated by projecting the data set corresponding to the fluctuating part of the velocity onto the calculated POD modes: $\boldsymbol{a^n} = \boldsymbol{\Psi}^T\boldsymbol{u^n}$, where $\boldsymbol{\Psi} = [\boldsymbol{\phi}^1\boldsymbol{\phi}^2 \cdots \boldsymbol{\phi}^N]$. The expansion of the fluctuating part of a snapshot n is obtained from

$$\boldsymbol{u}^{\boldsymbol{n}} = \sum_{i=1}^{N} a_i^n \boldsymbol{\phi^i} = \boldsymbol{\Psi a^n} \tag{3}$$

Equation (3) gives the best approximation of the data ensemble in the sense that the average least-squares truncation error is a minimum for any given number $m \leq N$ of basis functions over all possible sets of orthogonal basis functions (Cizmas et al. [31]). The ensemble-averaged energy of the fluctuating component is given by the sum of all of the eigenvalues:

$$\boldsymbol{E} = \sum_{i=1}^{N} \lambda^i \tag{4}$$

B. Convergence and Energy from Dominant Mode

The number of snapshots required to adequately capture the energy content for a given mode depends on the nature or complexity of the flow. Moreover, the amount of energy associated with a mode may not fully converge due to an insufficient number of snapshots. Breuer and Sirovich [32] applied the snapshot method to determine the eigenfunctions of a general class of linear operators from an ensemble of realizations that was derived from that system. It was observed that as the number of snapshots increases, the computed energy spectra approaches the analytical spectra and the fidelity of the snapshot procedure improves. Their results also showed that the eigenfunctions with less energy are more accurately resolved as the number of snapshot increases. Furthermore, the average error decreases as the number of snapshot increases. Cazemier et al. [33] applied the POD to analyze the velocity field for a cavity flow at a Reynolds number (based on cavity height) of 22,000. They reported that 700 snapshots were insufficient to obtain a fully converged eigenvalue corresponding to the first mode. Sen et al. [17] applied POD to their DNS results of fully developed channel flows over smooth and rough surfaces. For the smooth wall, the Reynolds number based on the friction velocity and channel half-height, $Re_\tau (= U_\tau h/\nu)$, was 180. In that study, $N = 6000$ realizations were used in the POD analysis.

To evaluate the sample size or number of snapshots necessary to perform the POD analysis in the present study, the fractional turbulent kinetic energy associated with the most dominant mode, $\lambda_1/\Sigma\lambda$, was computed for an increasing number of snapshots. The results for test SM (which corresponds to the upstream measurement plane P0 in test APG), CC-P1, FPG-P1, APG-P1, APG-P2, and APG-P3 are summarized in Table 2. As described in Sec. II.B, P1 is the measurement plane containing the rib, and P2 and P3 correspond to measurement planes in the redevelopment region. As the number of snapshots increases, the relative contribution of the first mode to the total energy $(\lambda_1/\Sigma\lambda)$ in the separated and reattachment region (tests CC-P1, FPG-P1, and APG-P1) as well as in the early region of flow redevelopment (APG-P2) consistently decreases until a threshold number is reached beyond which no further significant reduction is observed. In the case of test CC-P1, for example, $\lambda_1/\Sigma\lambda = 12.7 \pm 0.4\%$ for $N \geq 50$. At least 500 snapshots are required to reduce the percentage variation in $\lambda_1/\Sigma\lambda$ for test FPG-P1 to 0.2% (that is, $\lambda_1/\Sigma\lambda = 11.9 \pm 0.2\%$ for $N \geq 500$). For tests APG-P1 and APG-P2, a minimum of 50 and 250 snapshots, respectively, are necessary to reduce the percentage variation to a similar level. On the contrary, the values of $\lambda_1/\Sigma\lambda$ obtained from the first 250 snapshots for test SM and tests APG-P3 do not decrease consistently with increasing number of snapshots. In the case of test SM, the percentage differences for $10 \leq N \leq 2040$ is not particularly large, and for $N \geq 250$, $\lambda_1/\Sigma\lambda = 22.9 \pm 0.5\%$. One would conclude from Table 2 that in all cases, the percentage contribution of first mode to total energy vary a little (less than 1%) when $N = 500$ snapshots are used. Therefore, the $N = 1700$ (test CC-P1) and $N = 2040$ (tests SM, FPG-P1, APG-P1, APG-P2, and APG-P3) used in the subsequent analysis are sufficient to achieve converged results.

The number of snapshots used in the present study is comparable with those used in previous POD studies. For example, Alfonsi and Primavera [16] used 2000 snapshot for smooth-wall channel flow and Kostas et al. [9] used 1024 snapshots for the decomposition of their backward-facing step flow. In the smooth-wall data reported by Sen et al. [17], it was observed that the values of $\lambda_1/\Sigma\lambda$ vary less than 1% for $1000 \leq N \leq 6000$.

For the upstream test case (test SM) in which the channel walls are parallel and there was no rib on the bottom wall ($N = 2040$), the first POD mode contributed 23.41% of the total turbulent kinetic energy. This value is only 7% less than the value of 28.58% reported by Sen et al. [17]. Note that $Re_\tau = 780$ in the present case compared with $Re_\tau = 180$ in the study by Sen et al. [17]. It has been suggested that as the Reynolds number increases (and the flow becomes increasingly turbulent) there is a more even or uniform distribution of energy among the various modes. As a result, the value of $\lambda_1/\Sigma\lambda$ would decrease with increasing Re_τ as noted previously. Similarly, in the DNS analysis of a fully developed channel flow at $Re_h = 3200$, Moin and Moser [10] reported $\lambda_1/\Sigma\lambda = 32\%$. Their Re_h is one-fourth of the value for test SM and may explain the relatively higher value of $\lambda_1/\Sigma\lambda$ reported by Moin and Moser [10]. In their PIV study of backward-facing flow, Kostas et al. [9] also reported a

Table 2 Energy convergence for increasing number of snapshots of the first mode

	SM	CC-P1	FPG-P1	APG-P1	APG-P2	APG-P3
Snapshots N	$\lambda_1/\Sigma\lambda$, %	$\lambda_1/\Sigma\lambda$, %	$\lambda_1/\Sigma\lambda$, %	$\lambda_1/\Sigma\lambda$, %	$\lambda_1/\Sigma\lambda$, %	$\lambda_1/\Sigma\lambda$, %
10	23.39	20.21	27.63	23.50	34.12	30.88
20	24.21	14.46	19.56	16.95	28.04	23.21
50	19.16	13.03	18.36	11.12	23.06	17.81
100	19.91	13.50	16.59	9.95	18.77	18.17
250	20.29	12.94	13.68	10.89	16.86	20.71
500	23.05	12.58	12.27	10.99	16.65	18.81
1000	22.13	12.43	11.97	10.62	16.20	17.55
1500	22.62	12.36	11.70	11.05	15.89	17.53
1700	22.89	12.35	11.90	11.10	15.88	17.88
1800	23.16	——	11.89	11.09	15.94	17.79
2040	23.41	——	11.77	11.15	15.90	17.84

higher value of $\lambda_1/\Sigma\lambda = 47\%$ for $Re_k = 580$ than a value of $\lambda_1/\Sigma\lambda = 13\%$ for $Re_k = 4660$. It should be remarked that the flowfield studied by Kostas et al. [9] is not exactly the same as that studied in the present study. In the present test CC, for example, $Re_k = 2640$ and the reattached length was 10.4 compared with $4.8k$ and $6.8k$ for $Re_k = 580$ and 4660, respectively, in the study by Kostas et al. [9] Notwithstanding these differences, $\lambda_1/\Sigma\lambda = 12.4\%$ for the present test CC is not significantly different from $\lambda_1/\Sigma\lambda = 13\%$ for $Re_k = 4660$ experiments by Kostas et al. [9].

The value of $\lambda_1/\Sigma\lambda$ for the upstream flow (test SM) is nearly twice as large as those obtained in the separated and reattached region (tests CC-P1, FPG-P1, and APG-P1). The energy level associated with the first mode as well as the energy convergence is similar for the three test cases in the recirculation region (i.e., tests CC-P1, APG-P1, and FPG-P1). This is not surprising because, as reported by Shah [6] and Shah and Tachie [20], the flow dynamics in the recirculation region was dominated primarily by the separated shear layer and not strongly dependent on pressure gradient. Kostas et al. [9] reported an increase in energy and enstrophy as their flow at $Re_h = 4660$ evolved from the separated region to the reattachment region. For example, $\lambda_1/\Sigma\lambda$ increased from 13.11% in the separated region to 18.66% (representing a 42% increase) in the reattached region. It was argued that a decrease in energy in the separated region is associated with the more complex flow features in the separated region, which produced a more uniform distribution of energy among the various modes. In other words, the increased level of flow complexity in the separated region would result in a less efficient decomposition and would more evenly distribute the energy across the modes. The present results also show that as the flow develops downstream of the separated region, the flow becomes structurally less complex so that the energy content in mode 1 becomes substantially larger than those in the separated shear layer. For example, there are 40 and 60% increases in $\lambda_1/\Sigma\lambda$ as the flow evolved from APG-P1 (separated region) to APG-P2 (reattached region) and APG-P3 (redeveloping region),

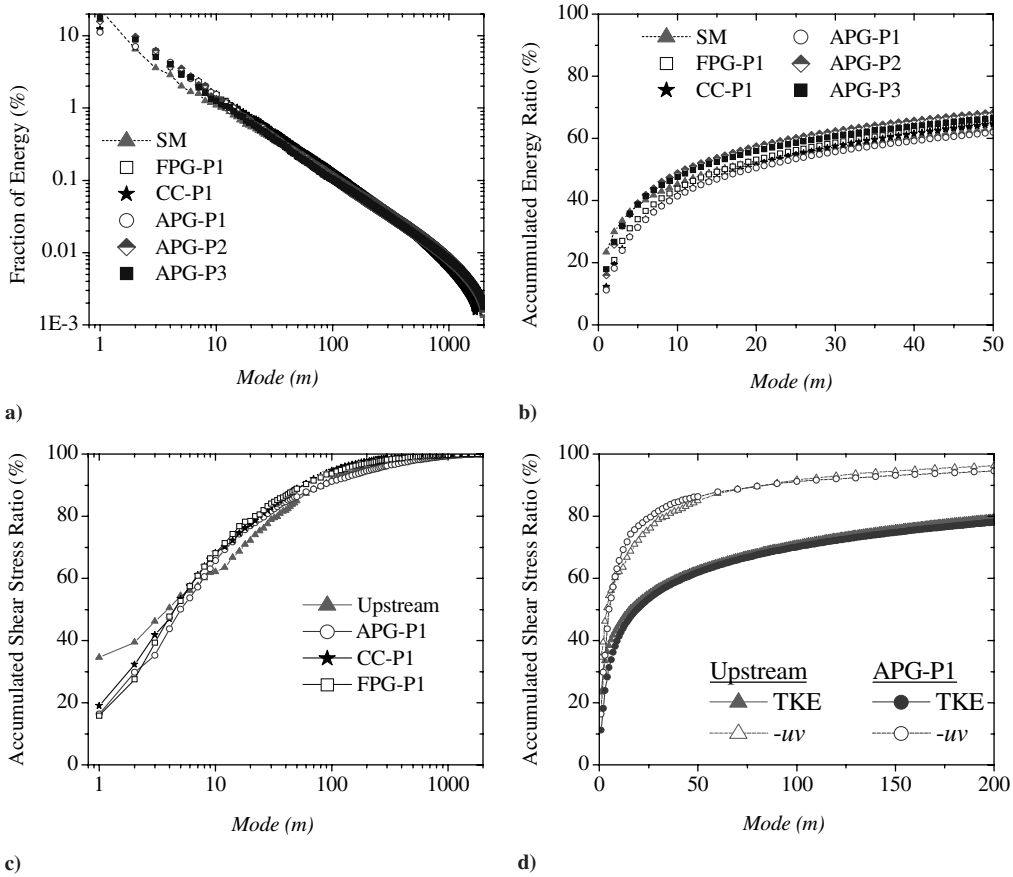

Fig. 4 Spectra of turbulent kinetic energy and Reynolds shear stress for various test cases: a) fractional contribution to the turbulent kinetic energy by the modes, b) accumulated turbulent kinetic energy ratio of modes as a function of modes, c) accumulated shear stress ratio as a function of modes, and d) comparison of accumulated turbulent kinetic energy ratio and shear stress as a function of modes.

Table 3 Reynolds shear convergence for increasing number of snapshots of the first mode

	SM	CC-P1	FPG-P1	APG-P1	APG-P2	APG-P3
Snapshots N	$\langle uv_1\rangle/\Sigma\langle uv\rangle$, %	$\langle uv_1\rangle/\Sigma\langle uv\rangle$, %	$\langle uv_1\rangle/\Sigma\langle uv\rangle$, %	$\langle uv_1\rangle/\Sigma\langle uv\rangle$, %	$\langle uv_1\rangle/\Sigma\langle uv\rangle$, %	$\langle uv_1\rangle/\Sigma\langle uv\rangle$, %
10	31.89	33.52	46.06	34.59	52.26	55.71
20	19.98	19.24	31.97	24.58	36.35	33.75
50	19.78	18.87	26.26	15.92	31.13	22.73
100	24.67	21.41	21.92	13.98	27.74	28.09
250	30.00	19.74	18.41	15.80	25.59	32.16
500	35.40	19.31	17.60	16.08	24.46	29.50
1000	33.12	18.93	16.17	15.23	23.93	27.35
1500	33.20	18.98	15.75	16.16	23.51	27.61
1700	33.88	19.07	16.00	16.27	23.19	28.28
1800	34.02	——	16.14	16.17	23.22	28.33
2040	34.36	——	15.80	16.50	23.34	28.52

respectively. Also note that the 40% increase in $\lambda_1/\Sigma\lambda$ from APG-P1 APG-P2 is consistent with a 42% increase reported by Kostas et al. [9] Furthermore, the $\lambda_1/\Sigma\lambda$ values in the redeveloping region are in closer agreement with the upstream value than those in the separated shear layer.

C. Spectra of Turbulent Kinetic Energy

Breuer and Sirovich [32] demonstrated that if the number of snapshots N were to exceed the resolution of the problem, spurious eigenvalues would be generated. If, on the other hand, the number of snapshots N were less than the number of spatial points M, all of the eigenvalues would provide a valid approximation to the analytical spectra of their system. However, as mentioned in Sec. IV.A, $M \gg N$ in the present case, which is also the fundamental reason for using the snapshot POD technique. The energy associated with each mode as well as the cumulative sum for the first 50 modes is plotted in Figs. 4a and 4b, respectively, to illustrate the effectiveness of the decomposition to capture energy in the upstream section (test SM), in the separated shear layer (tests CC-P1, APG-P1, and FPG-P1), and in the redevelopment region of the test APG (tests APG-P2 and APG-P3). An efficient decomposition will capture nearly 100% of the total energy with a relatively small number of modes. As expected, the energy associated with the modes decreases exponentially with increasing mode. Figure 4a reveals that for the first 900 modes, the spectra decay linearly with increasing mode but fall off beyond this limit. The energy magnitude drops two orders within the first 100 modes. This implies that most of the turbulent kinetic energy resides in the first 100 modes. For test CC the first 25 and 50 modes, respectively, contributed 50 and 65% of the total turbulent kinetic energy. These are comparable with the energy spectra for a backward-facing step reported by Kostas et al. [9]. They reported about 57% energy by mode 25 and 67% energy by mode 50 for their backward-facing step at the higher Reynolds number ($Re_k = 4660$). Consistent with the data presented in Table 2, a noticeable increase is observed in the energy level of the first mode for tests APG-P2 and APG-P3, which are downstream of the reattachment region. The convergence of the upstream flow is faster compared with the separated flow, but beyond mode 20, the convergence is nearly similar for all of the flows except for tests APG-P2 and APG-P3.

D. Spectra of Reynolds Shear Stress

Consideration is now turned to the contribution of the dominant modes to Reynolds shear stress. It should be recalled that the mean flow is represented by the zeroth mode. Therefore, $\partial U/\partial y$ is independent of the POD modes. Because the production of turbulent kinetic energy in quasi-two-dimensional turbulent flows is almost entirely given by $\langle -uv\rangle \partial U/\partial y$, the contribution of the dominant modes to the Reynolds shear stress is equivalent to the fractional contribution to the total energy production. Note that the formulation of the POD ensures that the characteristic eddies are those with maximal contribution to turbulent kinetic energy. In other words, the theory does not maximize the contribution of the dominant structures to the Reynolds shear stress and turbulence production.

Table 3 provides a summary of the relative contribution of the first mode to the total Reynolds shear stress for the various test cases analyzed in the previous section. The convergence of the Reynolds shear stress is observed to be qualitatively similar to that of the turbulent kinetic energy. For snapshots $N \geq 500$, less than 2% variation is observed in the values of $\langle uv_1\rangle/\Sigma\langle uv\rangle$. Similar to the observations made for the turbulent kinetic energy, $\langle uv_1\rangle/\Sigma\langle uv\rangle$ for the upstream test condition is higher than those in the separated shear layer. Moreover, the values in the redevelopment region are higher than those in the separated layer but somewhat lower than the upstream value. These results suggest that the relative contribution of mode 1 to the total Reynolds shear stress (and turbulence production) also decreases with increasing complexity in flow structure.

A comparison between the data presented in Tables 2 and 3 reveals that the contribution of the first mode to the Reynolds shear stress is much higher than the contribution to the turbulent kinetic energy. In test SM, for example, $\langle uv_1\rangle/\Sigma\langle uv\rangle = 34\%$ compared with $\lambda_1/\Sigma\lambda = 23\%$. In general, the values of $\langle uv_1\rangle/\Sigma\langle uv\rangle$ are approximately 45 to 60% larger than the corresponding $\lambda_1/\Sigma\lambda$ values. The higher contribution of the Reynolds shear stress compared with the turbulent kinetic energy by the first mode is in agreement with the findings of Moin and Moser [10]. The implications of these observations are that the characteristic large scales would contribute more efficiently to the Reynolds shear stress than they contribute to the normal stresses (or turbulent kinetic energy).

In Fig. 4c, the cumulative sum of the Reynolds shear stress as a function of modes is plotted and the cumulative sum of the Reynolds shear stress and the turbulent kinetic energy is compared in Fig. 4d. The shear stress converges faster for the first five modes at the upstream section than the other planes. Subsequently ($m > 5$), the convergence rate becomes similar for all test cases (Fig. 4c). No significant difference is observed between the three test cases in the separated shear layer.

For all of the test cases, the convergence of the Reynolds shear stress is faster than for the turbulent kinetic energy. At the upstream section, for example, 85% of the total Reynolds shear stress $\Sigma\langle uv\rangle$ is recovered by mode 50, whereas only 66% of turbulent kinetic energy E is recovered. It is interesting to note that this finding is similar to experimentally observed behavior of large eddies. Blackwelder and Kovasznay [34] found that the largest eddies in a turbulent boundary layer contribute proportionately more to Reynolds shear stress than to the turbulent kinetic energy.

E. POD Eigenfunctions

The POD eigenfunctions or modes represent the most common events occurring in the fluctuating field. Furthermore, the low-order modes are representative of the most energetic events in the flow (Bonnet and Delville [35]). The POD eigenfunctions ϕ_u (which correspond to streamwise velocity) in the lower half of the upstream section, test SM, are shown in Figs. 5a–5e. The corresponding eigenfunctions for test APG-P1 are shown in Figs. 5f–5j. The solid lines in Figs. 5f–5j represent the approximate location of the dividing streamline (which are presented by Shah [6] and Shah and Tachie [20]). The POD eigenfunctions show the presence of structures that

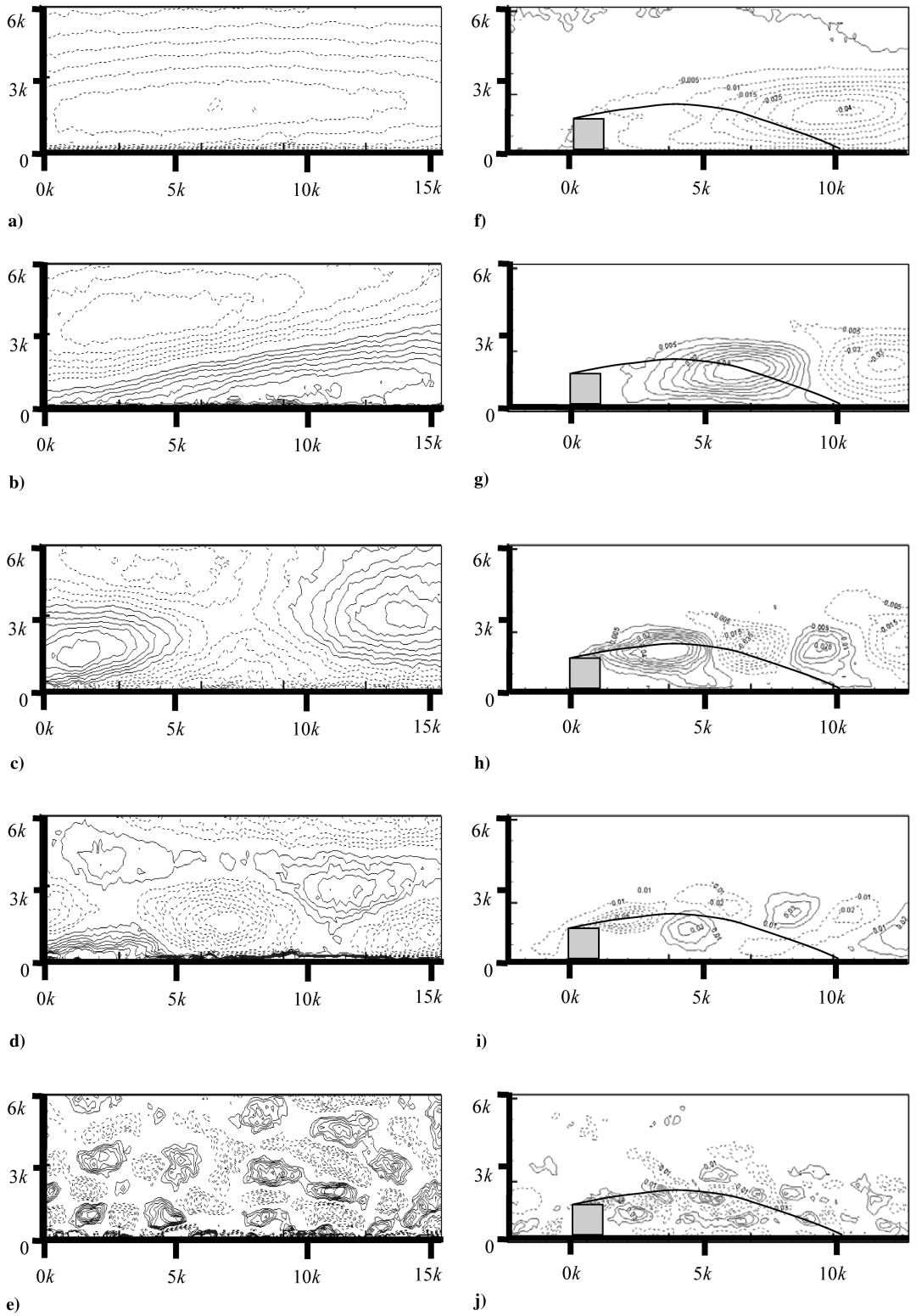

Fig. 5 Eigenfunctions ϕ_u of test SM for a) mode 1, b) mode 2, c) mode 5, d) mode 10, and e) mode 100 and of test APG-P1 for f) mode 1, g) mode 2, h) mode 5, e) mode 10, and j) mode 100. Note for test SM that the origin is arbitrarily taken at the lower left corner to show the extent of the structures.

are either positive or negative indicated by solid or dashed contour lines, respectively. For test SM, the eigenfunction associated with the first mode, ϕ_u^1, which possesses the most energy, is shown in Fig. 5a. In this figure, an elongated slightly inclined structure is observed close to the wall. The structure appears to be larger than the length of the measurement plane, which is $x/k \approx 15$. The structure in mode 1 is similar to that reported by Sen et al. [17] for their smooth-wall flow, and the relatively large size of the structure is indicative of the high contribution of large eddies (Cazemier et al. [33]). The eigenfunction associated with second mode, ϕ_u^2, also has a substantial amount of energy. Although these structures are also relatively large, they are smaller than in mode 1. A trend noticeable in the progression toward higher modes is the increase in small-scale structures within them. The small-scale structures (i.e., for ϕ_u^{100}), which are associated with higher order modes, are found to contribute only a small fraction to the turbulent kinetic energy. For example, it was observed that mode 100 only contributes 0.12% (Fig. 4a) to the total turbulent kinetic energy.

The eigenfunction associated with the most dominant mode, ϕ_u^1, shows a large structure that has the highest intensity in the vicinity of

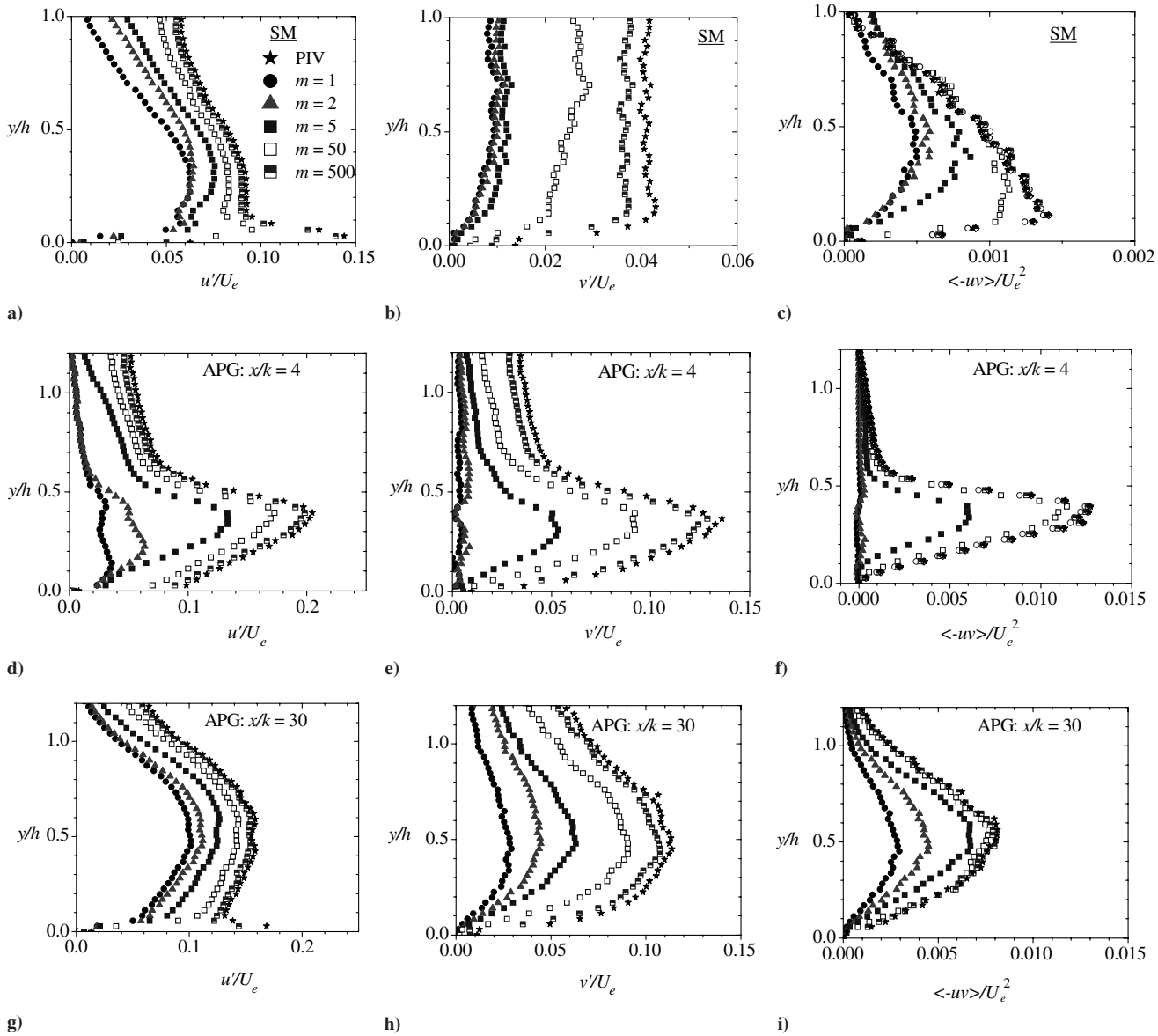

Fig. 6 Profiles of turbulent quantities for test SM and test APG obtained using various modes in reconstruction.

the reattachment region. A similar trend as in the case of test SM is also observed for the size of the structures in the case of APG-P1. It is important to note that very small and very large structures are never present in the same mode, due to the arrangement of eigenvalues from the highest energy to the lowest energy.

F. Reconstruction of the Turbulent Quantities

1. Turbulent Intensities and Reynolds Shear Stress

Low-order representations of the instantaneous velocity fields were constructed from various POD modes. From the reconstructed velocity fields, the corresponding turbulent intensities and Reynolds shear stress distributions were determined. Those results, together with the ensemble PIV contours, are presented and discussed in detail by Shah [6]. The plots qualitatively illustrate the cumulative effect of using increasingly more modes in the data reconstruction. It was observed that as the number of the modes is increased, a consistent progression toward the contours obtained from PIV data is observed. The POD reconstruction showed that the first few modes capture the energy in the region near and downstream of the reattachment. This would indicate that the flow dynamics in these regions are determined by large-scale structures. The results also showed that higher-order modes or relatively small-scale structures contribute to the peak of turbulent intensity along the mean separation streamline in the separated region for $x/k \leq 5$. Moreover, relatively fewer POD modes were required to reconstruct the Reynolds shears stress than are needed for the transverse turbulent intensity. The implication is that the dominant scales are more relevant to the dynamics of the Reynolds shear stress when compared with the transverse turbulent intensity. These observations are quantified next.

The profiles of turbulent intensities and Reynolds shear stress reconstructed from selected modes (i.e., 1, 2, 5, 50, and 500 POD modes) at selected streamwise locations are used to examine the number of modes necessary for the reconstructed profiles to collapse onto the corresponding profiles obtained from the PIV ensemble (or PIV profiles). The following selected locations and/or test cases are used: upstream section (test SM) and $x/k = 4$ and 30 for test APG. Plots for other test cases and x/k locations are available by Shah [6]. As mentioned earlier, the location $x/k = 4$ corresponds approximately to the center of the separation bubble, and $x/k = 30$ is in the redevelopment region.

For the upstream test condition (test SM) shown in Fig. 6a, the first few modes ($m \leq 5$) were not able to capture the sharp peak observed in the streamwise intensity profile close to the wall. Moreover, at these lower modes, the y location of $\langle -uv \rangle_{\max}$ is farther away from the wall than in the PIV profile. Overall, the agreement between the reconstructed profiles and the corresponding PIV profile improves as the number of mode m increases. For a given mode, the reconstructed

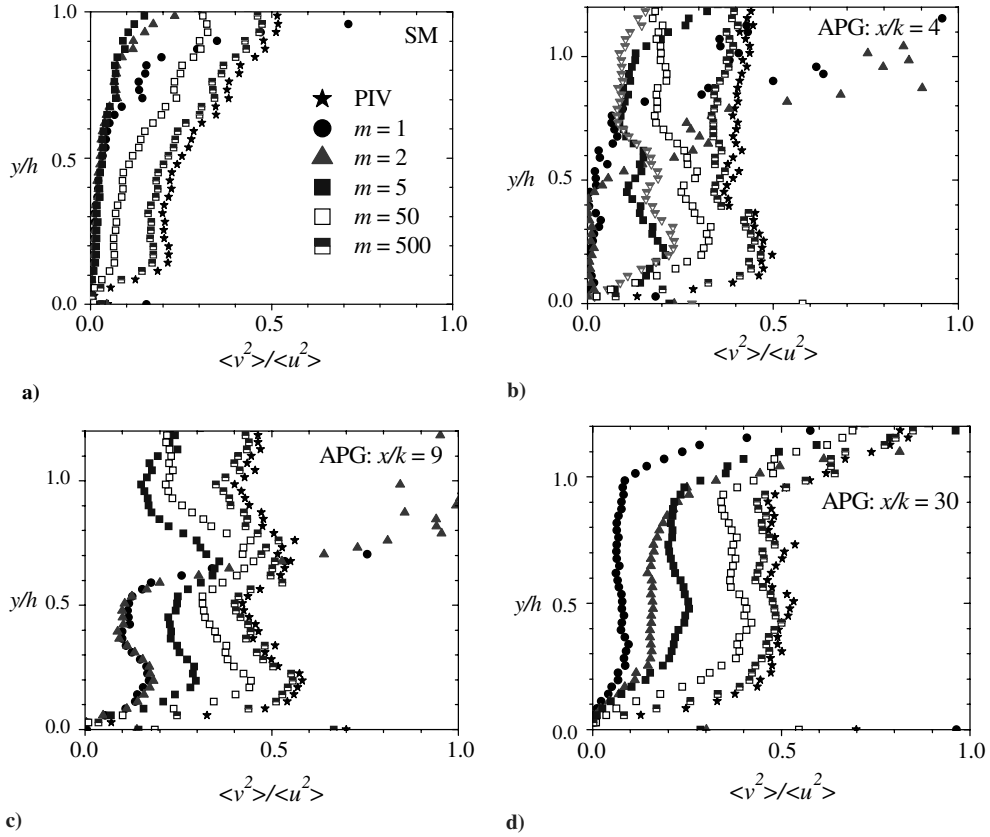

Fig. 7 Profiles of stress ratios $\langle v^2 \rangle / \langle u^2 \rangle$ obtained using various modes in reconstruction.

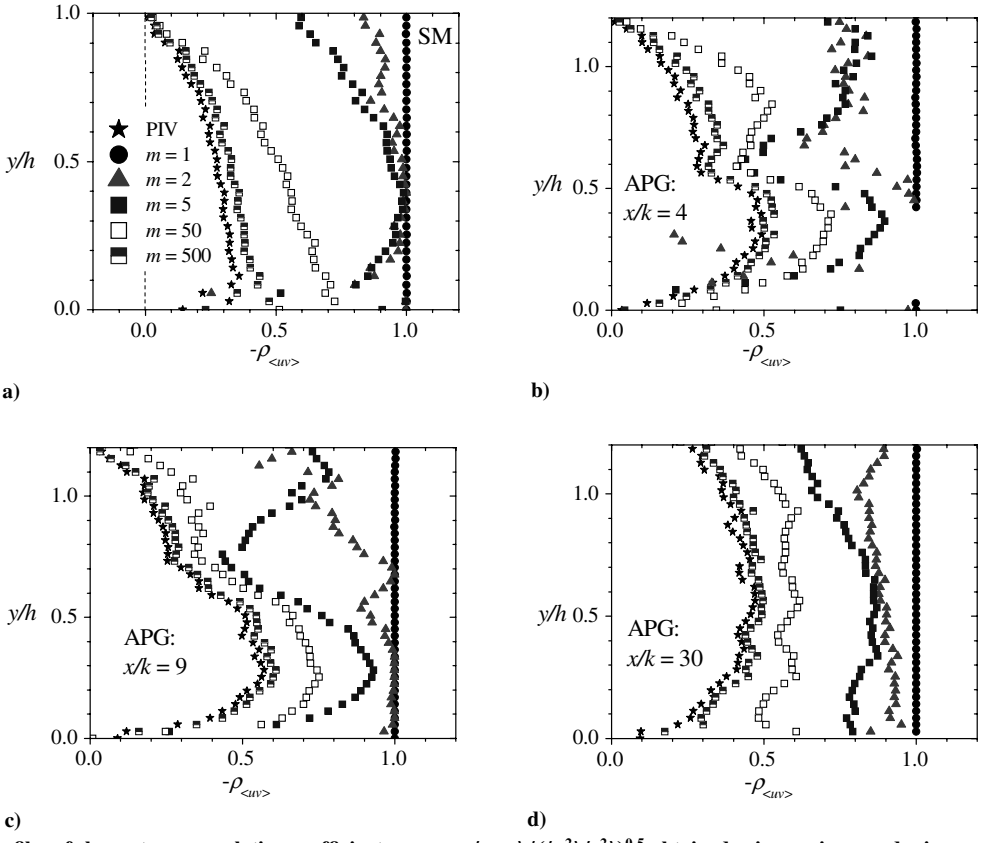

Fig. 8 Profiles of shear stress correlation coefficient $-\rho_{\langle uv \rangle} = \langle -uv \rangle / (\langle u^2 \rangle \langle v^2 \rangle)^{0.5}$ obtained using various modes in reconstruction.

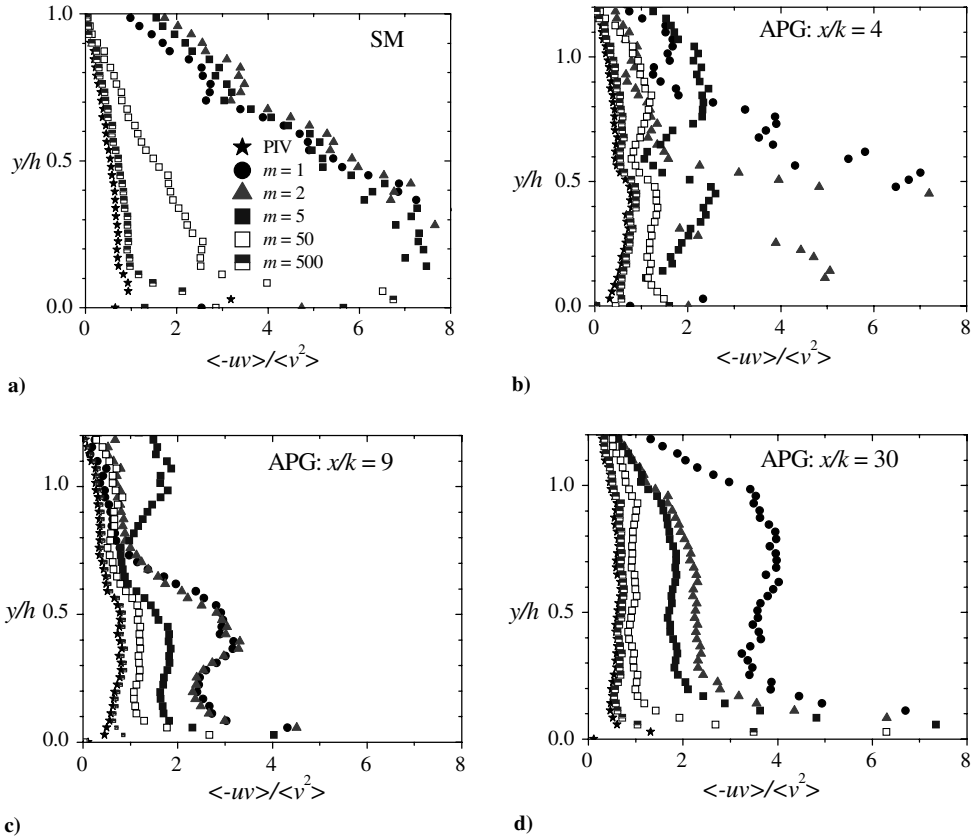

Fig. 9 Profiles of shear stress correlation coefficient $\langle -uv \rangle / \langle v^2 \rangle$ obtained using various modes in reconstruction.

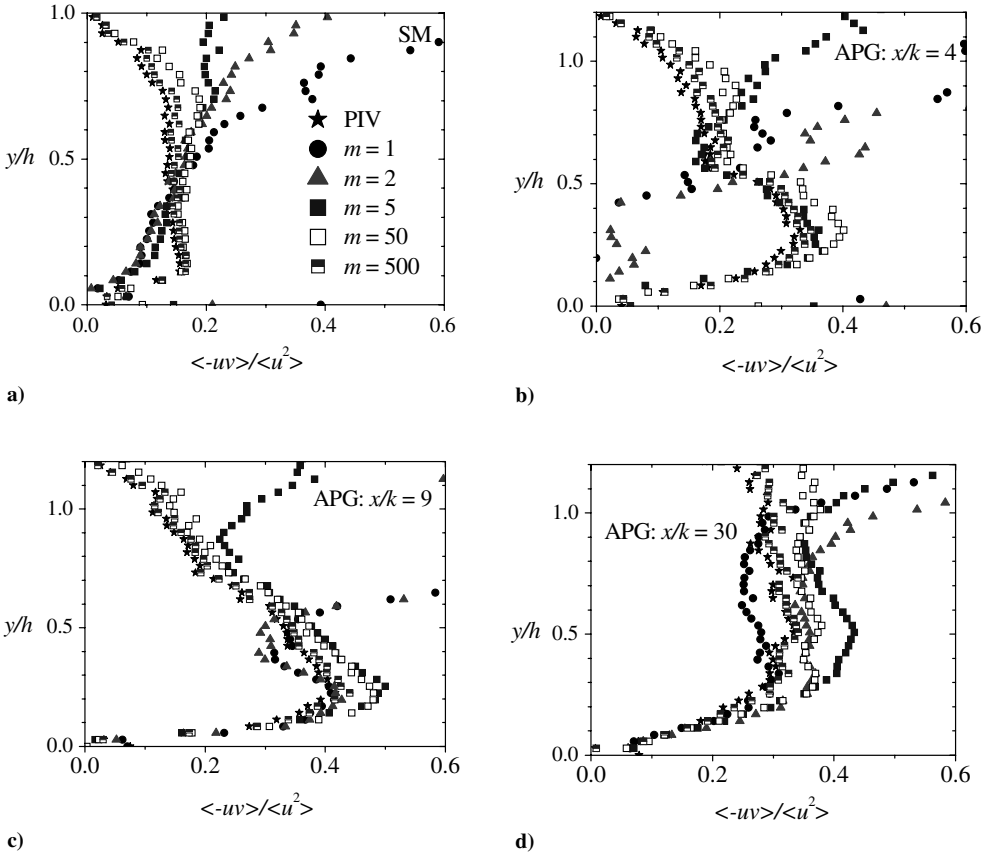

Fig. 10 Profiles of shear stress correlation coefficient $\langle -uv \rangle / \langle u^2 \rangle$ obtained using various modes in reconstruction.

profiles of the Reynolds shear stress (Fig. 6c) and streamwise turbulent intensity are closer to the corresponding PIV profiles than observed for the transverse turbulent intensity (Fig. 6b). The data presented in Figs. 6a–6c show that close to the channel centerline, nearly 80, 62, and 100% of u', v', and $\langle -uv \rangle$ obtained from the PIV were recovered by $m = 50$. Meanwhile, only 66, 48, and 76% of $u'_{\max}$, $v'_{\max}$, and $\langle -uv \rangle_{\max}$ from the PIV were recovered by $m = 50$. By 500 modes, the Reynolds shear stress collapsed very well onto the PIV data, but the reconstructed values of v' are still significantly smaller than the corresponding PIV data.

The profiles obtained in the separated shear layer (at $x/k = 4$) and plotted in Figs. 6d–6f show similar trends to those observed at the upstream location. When profiles at $x/k = 4$ and 9 (not shown) of test APG in the separated region are compared, it was observed that the reconstructed profiles at $x/k = 4$ showed a slower tendency to collapse onto the PIV ensemble than profiles at $x/k = 9$. For example, at $x/k = 9$, the distinct peak values observed in u', v', and $\langle -uv \rangle$ from the PIV data are already noticeable by modes 1 and 2. On the other hand, $m \geq 5$ modes are required to clearly reveal the dominant peaks at $x/k = 4$. Similar to the observation made at the upstream location, fewer number of POD modes are required to collapse the reconstructed Reynolds shear stress on to the PIV profile in comparison with the turbulent intensities (or Reynolds normal stresses). These results provide additional support to earlier observation that irrespective of the test condition or location, the large scales contribute more effectively to the Reynolds shear stress than they contribute to the turbulent kinetic energy or Reynolds normal stresses. Unlike the upstream location, however, the POD modes required to collapse the transverse turbulent intensity is not any larger than needed for the streamwise turbulent intensity profiles. The observed differences in the v' distributions in the upstream and shear layer are likely due to the large values of V (and $\partial V/\partial y$) in the separated shear layer than at the upstream location. As explained by Shah [6], the large values of $\partial V/\partial y$ would contribute to the production of $\langle v^2 \rangle$ in the separated shear layer, whereas the negligible values of $\partial V/\partial y$ at the upstream location would imply that $\langle v^2 \rangle$ would only benefit from energy redistribution via $\langle u^2 \rangle$.

In Figs. 6g–6i, the trends observed in the turbulent intensities and Reynolds shear stress in the redevelopment region are qualitatively similar to those made in the separated shear layer and at the upstream location. In the redevelopment region, however, v' also required fewer POD modes to collapse onto the PIV data when compared with the distributions reported for the upstream location. It is expected that as the flow develops further downstream and the magnitude of V (and

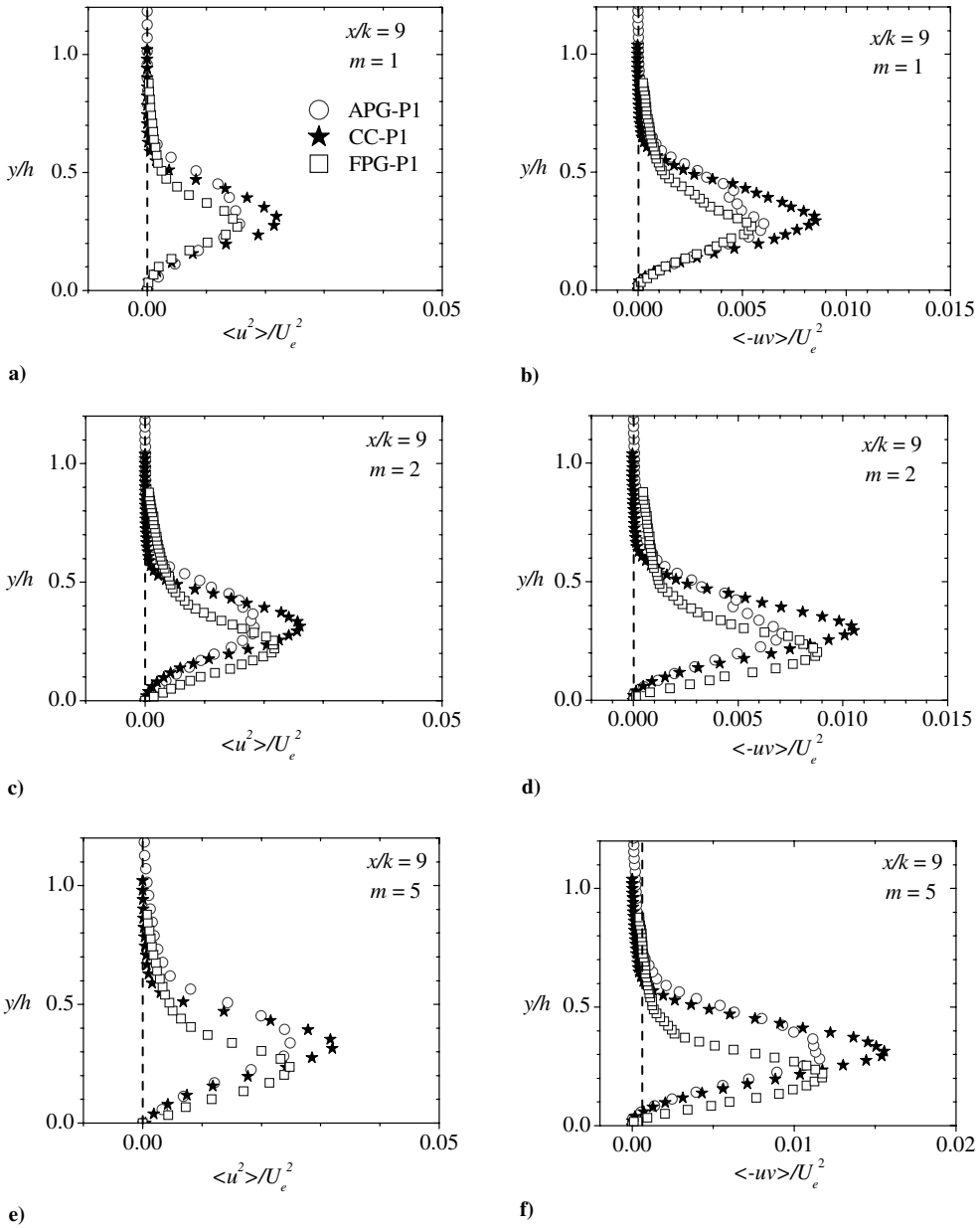

Fig. 11 Comparison of various test conditions reconstructed from modes 1, 2, and 5 at $x/k = 9$.

$\partial V/\partial y$) decrease to a level observed at the upstream location, increasingly more modes would be necessary for v' to collapse onto the PIV data.

2. *Reynolds Stress Ratios from Various POD Modes*

In the previous section, it was argued that the large scales, in general, contribute most effectively to the Reynolds shear stress and least to the transverse turbulent intensity. Those observations are further quantified in this section by comparing the stress ratios from an increasing number of POD modes with those obtained from the PIV data. Note that the stress ratios also provide useful information on the large-scale anisotropy and energy redistribution mechanism. Figures 7 and 8, respectively, show profiles of the Reynolds normal stress ratio $\langle v^2\rangle/\langle u^2\rangle$ and the correlation coefficient $-\rho_{\langle uv\rangle}$ from modes $m = 1$, 2, 5, 50, and 500 to the PIV data. The largest scales (which correspond to the lower values of m) contribute more significantly to the streamwise component than to the transverse component. This observation is valid for all test conditions and/or locations. At the upstream location and $x/k = 4$, for example, $\langle v^2\rangle/\langle u^2\rangle \approx 0.2$ and 0.5, respectively, in the region $y/h < 0.5$. With an increasing number of POD modes, the importance of large scales diminishes and the contribution from the smaller scales increases. The results presented in Fig. 7 imply that the larger scales are relatively more important to the dynamics of $\langle u^2\rangle$ than for $\langle v^2\rangle$. Conversely, the relatively smaller scales would play a more significant role in the dynamics of $\langle v^2\rangle$ than for $\langle u^2\rangle$. Figure 8 reveals that the large scales are more strongly correlated than the small scales. This observation is based on the premise that the magnitude of the correlation coefficient decreases with increasing POD mode (decreasing size of coherent structure). At mode 1, for example, a near-perfect correlation ($-\rho_{\langle uv\rangle} \approx 1$) was observed across the channel.

The ratios of the Reynolds shear stress to the normal stresses ($\langle -uv\rangle/\langle v^2\rangle$ and $\langle -uv\rangle/\langle u^2\rangle$) are shown in Figs. 9 and 10, respectively. When the overall contributions from the small and large scales to the Reynolds stresses are considered, it is observed that $\langle -uv\rangle/\langle v^2\rangle < 1$, as evident from the PIV data at all test locations. On

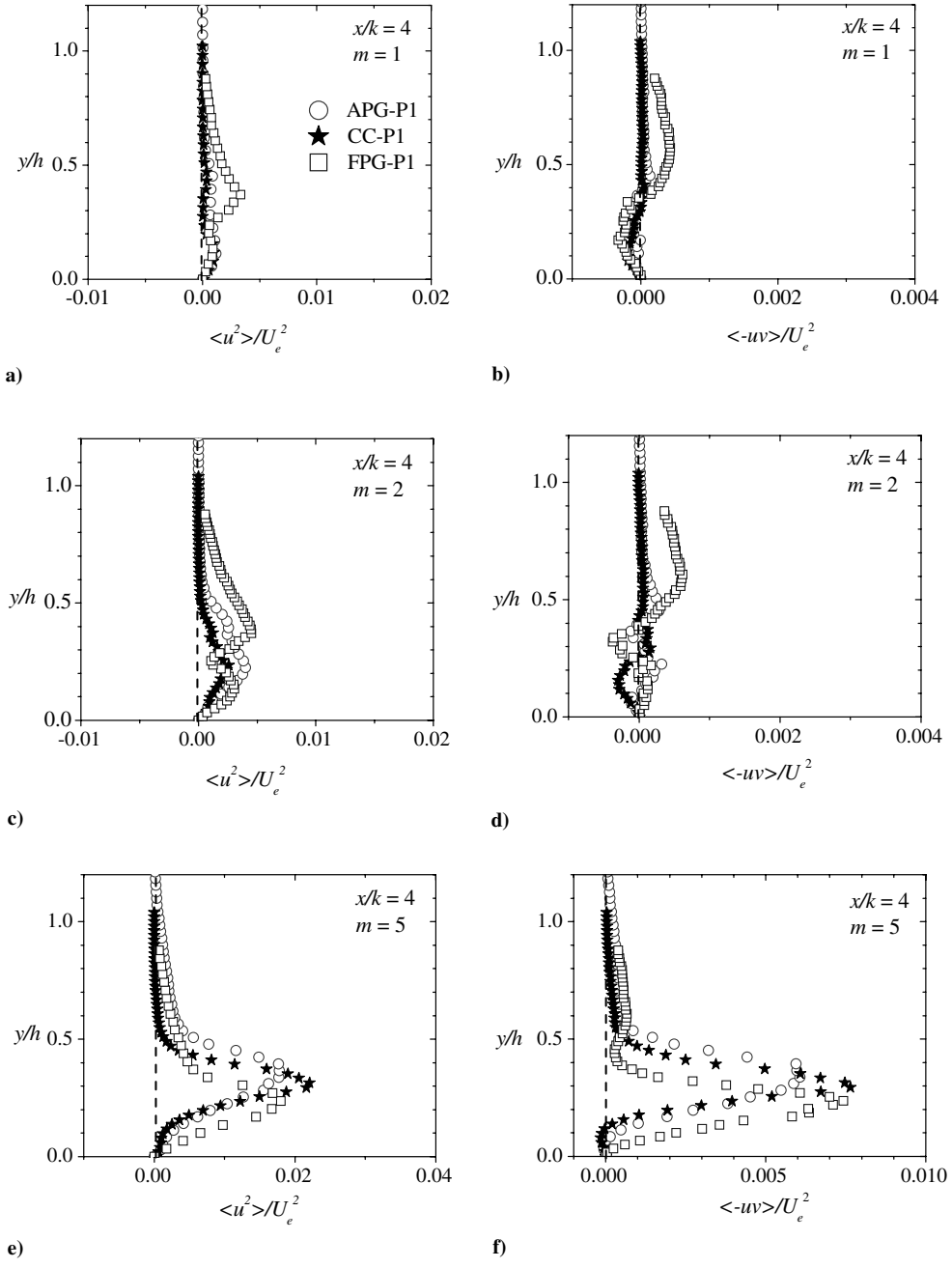

Fig. 12 Comparison of various test conditions reconstructed from modes 1, 2, and 5 at $x/k = 4$.

the other hand, the large scales contribute more effectively to the shear stress ($\langle -uv \rangle$) than to transverse normal stress ($\langle v^2 \rangle$) so that $\langle -uv \rangle / \langle v^2 \rangle$ is generally larger than unity for lower POD modes. In the region $y/h < 0.4$ at the upstream location, for example, $\langle -uv \rangle / \langle v^2 \rangle = 7.5$ for the first five POD modes. The contributions from the lower POD modes to $\langle -uv \rangle$ and $\langle u^2 \rangle$ are relatively more complex than observed in the prior plots. At the upstream location, for example, the first 10 modes ($m \leq 10$) contribute more to $\langle u^2 \rangle$ than to $\langle -uv \rangle$ in the region $y/h \leq 0.4$. The reverse observation is made in the outer part of the channel ($y/h > 0.4$). A similar observation is also made at for $m = 2$ at $x/k = 5$.

3. Pressure Gradient Effects on Reynolds Stresses from Mode 1

The reconstructed Reynolds stresses $\langle u^2 \rangle$ and $\langle -uv \rangle$ from modes 1, 2, and 5 at $x/k = 4$ and 9 for the three test cases are compared to study the effects of pressure gradients on the POD decomposition in the separated shear layer. The profiles obtained at $x/k = 9$ (Fig. 11) using modes 1, 2, and 5 are qualitatively similar to those obtained from the PIV data (see Fig. 2 and also Shah [6] and Shah and Tachie [20]). For example, the peak values for test CC are relatively higher than those obtained in test APG. The turbulence levels for the first few modes are also not substantially different from the corresponding PIV ensemble. This is consistent with the notion that the isocontour plots of the Reynolds stresses from the first few modes capture the energy around the downstream region (Shah [6]). As in the PIV data, the $\langle -uv \rangle$ profiles at $x/k = 9$ are positive in the region $y/h < 0.5$. In contrast, the magnitudes of $\langle u^2 \rangle$ and $\langle -uv \rangle$ from modes 1 and 2 at $x/k = 4$ (see Fig. 12) are only a small fraction of the corresponding values obtained from the PIV ensemble. Furthermore, the profiles from these modes also do not follow the pressure gradient trends observed in the PIV data at $x/k = 4$ and 9. More important, regions of negative $\langle -uv \rangle$ are observed in the lower half of the channel at $x/k = 4$. By mode 5, the turbulence levels and the sign of $\langle -uv \rangle$ become similar to the PIV data. These results are further evidence that the profiles at $x/k = 4$ showed a slower tendency to collapse onto the PIV ensemble than those at $x/k = 9$.

V. Conclusions

Turbulent flow downstream of a transverse square rib in pressure gradients is presented. The mean velocity profiles were distorted substantially downstream of the rib. In the separated region, the separated shear layer produced by the ribs dominates the dynamics of the flow. Far downstream in the redevelopment region, however, pressure gradient effects dominate. In the separated region, the distribution of mixing length in the inner region does not follow the well-documented linear profile reported for simple near-wall turbulent flows. This suggests that turbulence models making such assumptions may not be able to accurately model the flow in this region. Even though a linear distribution of the mixing length is observed in the early stage of flow redevelopment, the slope was nearly twice as large as those in canonical turbulent flows. The slope of eddy viscosity in the near-wall region was observed to increase continuously for $x/k < 30$. Meanwhile, the eddy viscosity also increased in the outer part of the flow in the same region but began to decay further downstream.

The results also show that contribution from the first dominant mode to the turbulent kinetic energy and Reynolds shear stress is higher at the upstream section than in the separated layer. This was attributed to a more uniform distribution of energy among the POD modes in the relatively more complex separated shear layer than in the upstream section. The contribution of the first mode to the Reynolds shear stress was greater than the contribution to the turbulent kinetic energy. A single large structure was observed for mode 1 for tests SM and APG-P1 that is responsible for the highest energy fraction. As the number of modes increased, the eigenfunctions show a progression toward small-scale structures. The reconstructed turbulent intensities, Reynolds shear stress as well the ratios of the Reynolds stress show that the large-scale structures contribute most to the Reynolds shear stress and least to transverse normal stress.

References

[1] Bradshaw, P., and Wong, F. Y. F., "The Reattachment and Relaxation of a Turbulent Shear Layer," *Journal of Fluid Mechanics*, Vol. 52, 1972, pp. 113–135. doi:10.1017/S002211207200299X

[2] Abu-Mulaweh, H. I., "Turbulent Mixed Convection Flow over a Forward-Facing Step—The Effect of Step Height," *International Journal of Thermal Sciences*, Vol. 44, No. 2, 2005, pp. 155–162. doi:10.1016/j.ijthermalsci.2004.08.001

[3] Abdalla, I. E., Cook, M. J., and Yang, Z., "Numerical Study of Transitional Separated-Reattached Flow over Surface-Mounted Obstacles Using Large-Eddy Simulation," *International Journal for Numerical Methods in Fluids*, Vol. 54, 2007, pp. 175–206. doi:10.1002/fld.1396

[4] Ruderich, R., and Fernholz, H. H., "An Experimental Investigation of a Turbulent Shear Flow with Separation, Reverse Flow and Reattachment," *Journal of Fluid Mechanics*, Vol. 163, 1986, pp. 283–322. doi:10.1017/S0022112086002306

[5] Kiya, M., and Sasaki, K., "Structure of Turbulent Separation Bubble," *Journal of Fluid Mechanics*, Vol. 137, 1983, pp. 83–113. doi:10.1017/S002211208300230X

[6] Shah, M. K., "Effects of Pressure Gradients on Separated and Reattached Flows," Ph.D. Dissertation, Dept. of Mechanical and Manufacturing, Univ. of Manitoba, Winnipeg, Canada, 2008.

[7] Shah, M. K., and Tachie, M. F., "PIV Investigation of Flow over a Transverse Square Rib in Pressure Gradients," 5th AIAA Theoretical Fluid Mechanics Conference, Seattle, WA, AIAA Paper 2008-4347, June 2008.

[8] Kline, S. J., Reynolds, W. C., Schraub, F. A., and Runstadler, P. W., "The Structure of Turbulent Boundary Layers," *Journal of Fluid Mechanics*, Vol. 30, 1967, pp. 741–773. doi:10.1017/S0022112067001740

[9] Kostas, J., Soria, J., and Chong, M. S., "A Comparison Between Snapshot POD Analysis of PIV Velocity and Vorticity Data," *Experiments in Fluids*, Vol. 38, 2005, pp. 146–160. doi:10.1007/s00348-004-0873-4

[10] Moin, P., and Moser, R., "Characteristic-Eddy Decomposition of Turbulence in a Channel," *Journal of Fluid Mechanics*, Vol. 200, 1989, pp. 471–509. doi:10.1017/S0022112089000741

[11] Lumley, J. L., "The Structure of Inhomogeneous Turbulent Flow," *Atmospheric Turbulence and Radio Wave Propagation*, edited by A. M. Yaglon, and V. I. Tatarski, Nauka, Moscow, 1967, pp. 167–178.

[12] Sirovich, L., "Turbulence and the Dynamics of Coherent Structures, Part 1: Coherent Structures," *Quarterly of Applied Mathematics*, Vol. 45, 1987, pp. 561–571.

[13] Berkooz, G., Holmes, P., and Lumley, J. L., "The Proper Orthogonal Decomposition in the Analysis of Turbulent Flows," *Annual Review of Fluid Mechanics*, Vol. 25, 1993, pp. 539–575. doi:10.1146/annurev.fl.25.010193.002543

[14] Kostas, J., "An Experimental Investigation of the Structure of a Turbulent Backward Facing Step Flow," Ph.D. Dissertation, Dept. of Mechanical Engineering, Monash Univ., Melbourne, Australia, 2002.

[15] Reichert, R. S., Hatay, F. F., Birigen, S., and Huser, A., "Proper Orthogonal Decomposition Applied to Turbulent Flow in a Square Duct," *Physics of Fluids*, Vol. 6, 1994, pp. 3086–3092. doi:10.1063/1.868133

[16] Alfonsi, G., and Primavera, L., "Dynamics of POD Modes in Wall Bounded Turbulent Flow," *Proceedings of the Royal Society of London A*, Vol. 463, 2007, pp. 593–612. doi:10.1098/rspa.2006.1785

[17] Sen, M., Bhaganagar, K., and Juttijudata, V., "Application of Proper Orthogonal Decomposition (POD) to Investigate a Turbulent Boundary Layer in a Channel with Rough Walls," *Journal of Turbulence*, Vol. 8, No. 41, 2007, pp. 1–21. doi:10.1080/14685240701615960

[18] Kostas, J., Soria, J., and Chong, M. S., "Particle Image Velocimetry Measurements of a Backward-Facing Step Flow," *Experiments in Fluids*, Vol. 33, 2002, pp. 838–853.

[19] Orrelano, A., and Wengle, H., "POD Analysis of Coherent Structures in Forced Turbulent Flow over a Fence," *Journal of Turbulence*, Vol. 2, No. 8, 2001, pp. 1–35. doi:10.1088/1468-5248/2/1/008

[20] Shah, M. K., and Tachie, M. F., "Flow Relaxation Past a Transverse Square Rib in Pressure Gradients," *AIAA Journal*, Vol. 46, No. 7, 2008, pp. 1849–1863. doi:10.2514/1.35528

[21] Prasad, A. K., Adrian, R. J., Landreth, C. C., and Offutt, P. W., "Effect of

Resolution on the Speed and Accuracy of Particle Image Velocimetry Interrogation," *Experiments in Fluids*, Vol. 13, 1992, pp. 105–116. doi:10.1007/BF00218156

[22] Forliti, D. J., Strykowski, P. J., and Debatin, K., "Bias and Precision Errors of Digital Particle Image Velocimetry," *Experiments in Fluids*, Vol. 28, 2000, pp. 436–447. doi:10.1007/s003480050403

[23] Coleman, H. W., and Steele, W. G., "Engineering Application of Experimental Uncertainty Analysis," *AIAA Journal*, Vol. 33,No. 10, 1995, pp. 1888–1896. doi:10.2514/3.12742

[24] Purtell, L. P., Klebnoff, P. S., and Buckley, F. T., "Turbulent Boundary Layer at Low Reynolds Number," *Physics of Fluids*, Vol. 24, 1981, pp. 802–811. doi:10.1063/1.863452

[25] Shah, M. K., and Tachie, M. F., "PIV Study of Turbulent Flow in Asymmetric Converging and Diverging Channel Flows," *Journal of Fluids Engineering*, Vol. 130, 2008, p. 011204. doi:10.1115/1.2829590

[26] Tachie, M. F., Balachandar, R., and Bergstrom, D. J., "Open Channel Boundary Layer Relaxation Behind a Forward Facing Step at Low Reynolds Numbers," *Journal of Fluids Engineering*, Vol. 123, 2001, pp. 539–544. doi:10.1115/1.1383971

[27] Eaton, J. K., and Johnston, J. P., "A Review of Research on Subsonic Turbulent Flow Reattachment," *AIAA Journal*, Vol. 19, No. 9, 1981, pp. 1093–1100. doi:10.2514/3.60048

[28] Wilcox, D. C., *Turbulence Modeling for CFD*, 2nd ed., DCW Industries, La Cãnada, CA, 2004.

[29] Johnson, D. A., and King, L. S., "A Mathematical Simple Turbulence Closure Model for Attached and Separated Boundary Layers," *AIAA Journal*, Vol. 23, No. 11, 1985, pp. 1684–1992. doi:10.2514/3.9152

[30] Meyer, E. K., Pedersen, J. M., and Özcan, O., "A Turbulent Jet in Crossflow Analysed with Proper Orthogonal Decomposition," *Journal of Fluid Mechanics*, Vol. 583, 2007, pp. 199–227. doi:10.1017/S0022112007006143

[31] Cizmas, P. G., Palacious, A., Brien, T. O., and Syamlal, M., "Proper Orthogonal Decomposition of Spatio-Temporal Patterns in Fluidized Beds," *Chemical Engineering Science*, Vol. 58, No. 19, 2003, pp. 4417–4427. doi:10.1016/S0009-2509(03)00323-3

[32] Breuer, K. S., and Sirovich, L., "The Use of Karhunen-Loève Procedure for the Calculation of Linear Eigenfunctions," *Journal of Computational Physics*, Vol. 96, 1991, pp. 277–296. doi:10.1016/0021-9991(91)90237-F

[33] Cazemier, W., Verstappen, R. W. C. P., and Veldman, A. E. P., "Proper Orthogonal Decomposition and Low-Dimensional Models for Driven Cavity Flows," *Physics of Fluids*, Vol. 10, 1998, pp. 1685–1699. doi:10.1063/1.869686

[34] Blackwelder, R. F., and Kovasznay, L. S. G., "Large-Scale Motion of a Turbulent Boundary Layer During Relaminarization," *Journal of Fluid Mechanics*, Vol. 53, 1972, pp. 61–83. doi:10.1017/S0022112072000047

[35] Bonnet, J.-P., and Delville, J., "Review of Coherent Structures in Turbulent Free Shear Flows and Their Possible Influence on Computational Methods," *Flow, Turbulence and Combustion*, Vol. 66, No. 4, 2001, pp. 333–353. doi:10.1023/A:1013518716755

N. Chokani
Associate Editor